Applied Physics Letters

Superconducting qubits in a flip-chip architecture

Cite as: Appl. Phys. Lett. **118**, 232602 (2021); https://doi.org/10.1063/5.0050173
Submitted: 12 March 2021 • Accepted: 24 May 2021 • Published Online: 10 June 2021

C. R. Conner, A. Bienfait, H.-S. Chang, et al.

AIP Publishing

Applied Physics Letters ARTICLE scitation.org/journal/apl

Superconducting qubits in a flip-chip architecture

Cite as: Appl. Phys. Lett. **118**, 232602 (2021); doi: 10.1063/5.0050173
Submitted: 12 March 2021 · Accepted: 24 May 2021 ·
Published Online: 10 June 2021

C. R. Conner,[1] A. Bienfait,[1,a)] H.-S. Chang,[1] M.-H. Chou,[1,2] É. Dumur,[1,3,b)] J. Grebel,[1] G. A. Peairs,[1,4] R. G. Povey,[1,2] H. Yan,[1] Y. P. Zhong,[1,c)] and A. N. Cleland[1,3,d)]

AFFILIATIONS

[1]Pritzker School of Molecular Engineering, University of Chicago, Chicago, Illinois 60637, USA
[2]Department of Physics, University of Chicago, Chicago, Illinois 60637, USA
[3]Institute for Molecular Engineering and Materials Science Division, Argonne National Laboratory, Lemont, Illinois 60439, USA
[4]Department of Physics, University of California—Santa Barbara, Santa Barbara, California 93106, USA

[a)]**Present address:** Université de Lyon, ENS de Lyon, Université Claude Bernard, CNRS, Laboratoire de Physique, F-69342 Lyon, France.
[b)]**Present address:** Université Grenoble Alpes, CEA, INAC-Pheliqs, QuantECA, 38000 Grenoble, France.
[c)]**Present address:** Shenzhen Institute for Quantum Science and Engineering, Southern University of Science and Technology, Shenzhen 518055, China
[d)]**Author to whom correspondence should be addressed:** anc@uchicago.edu

ABSTRACT

Flip-chip architectures have recently enabled significant scaling-up of multi-qubit circuits and have been used to assemble hybrid quantum systems that combine different substrates, for example, for quantum acoustics experiments. The standard flip-chip method uses superconducting galvanic connections between two substrates, typically implemented using sophisticated indium wafer-bonding systems, which give highly reliable and temperature-cyclable assemblies, but are expensive, somewhat inflexible in design, and require robust substrates that can sustain the large compressive forces required to cold-weld the indium bonds. A much simpler method is to assemble dies using very low-force contacts and air-dried adhesives, although this does not provide a galvanic contact between the dies. Here, we demonstrate that the latter technique can be used to reliably couple superconducting qubit circuits, in which the qubits are on separate dies, without the need for a galvanic connection. We demonstrate full vector qubit control of each qubit on each of the two dies, with high-fidelity single-shot readout, and further demonstrate entanglement-generating excitation swaps as well as benchmark a controlled-Z entangling gate between the two qubits on the two dies. This exemplifies a simple and inexpensive assembly method for two-plus-one-dimensional quantum circuit integration that supports the use of delicate or unusually shaped substrates.

Superconducting qubits are a promising platform for the realization of quantum computing technologies.[1–3] As the size and complexity of superconducting quantum processors increases, the need for more flexible architectures and increased connectivity has grown.[4–7] Achieving sufficient connectivity can be achieved using through-chip vias[8,9] or flip-chip assemblies with cold-welded indium bump bonding.[10] These sophisticated methods require expensive tooling inaccessible to most academic researchers. To address these challenges, we have previously developed and described a facile flip-chip fabrication process,[11] originally conceived and developed for coupling superconducting qubit circuits to quantum acoustic systems and other hybrid applications. Here, we expand on this technique and demonstrate that it can also serve for the high-fidelity coupling of superconducting qubit circuits, each circuit fabricated on a separate die, without the need for a galvanic connection between the dies. This holds promise for the simple and rapid expansion of qubit circuit complexity, allowing wiring in two-plus-one dimensions and, thereby, alleviating qubit interconnect challenges.

The device measured in this work is shown in Fig. 1. The device comprises two double-side polished sapphire dies, where at least one die must be transparent, a larger control die with qubit $Q1$ shown prior to assembly in panel (a), and a second smaller die with qubit $Q2$ shown in panel (c), with the assembled dies shown in panel (b), with the smaller die outlined in red. The dies are assembled using a mask

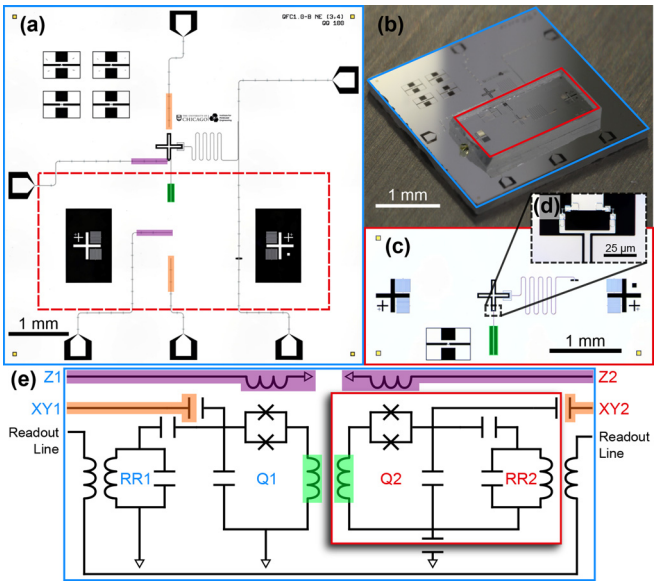

FIG. 1. Die design and assembly. (a) Micrograph of the larger (control) die, with a single xmon qubit *Q*1 along with its control lines, readout resonator, and readout transmission line. Also on this die are the control lines for qubit *Q*2 which is located on the other die, shown in panel (c). Red outline shows location of second die, and SU-8 spacers and adhesive are in the dark rectangles on the left and right sides of that outline. The inter-qubit coupling waveguide is highlighted in green. XY and Z control lines are highlighted in orange and purple, respectively. (b) Assembled stack with the control die in (a) outlined in blue and the smaller flipped die in (c) outlined in red. (c) Micrograph of smaller flipped die, containing a second xmon qubit *Q*2 with its coupling inductor (green) and readout resonator. All control and readout lines are located on the control die. Top die is flipped along its horizontal axis to align with bottom die. (d) Detail of the SQUID loop for *Q*2. (e) Equivalent circuit for the two-qubit system, showing qubits *Q*1 and *Q*2, the qubit *XY* and *Z* control lines as well as the capacitively coupled readout resonators *RR*1 and *RR*2 probed by the readout line. The larger control die is outlined in blue and the smaller flipped die in red. Color overlays match those in panels (a) and (c).

aligner, achieving horizontal alignment better than 2 μm using alignment marks (see Fig. 1). Vertical spacing is set by 7 μm high SU-8 photodefined spacers, and dies are attached using photoresist as an adhesive, which is briefly cured with a hot-air gun; spacer height is verified by profilometry and assembled spacing by electron microscopy. Qubits and control wiring are patterned in aluminum, with Josephson junctions fabricated using the Dolan technique,[12] using qubits with two small-area Josephson junctions in a superconducting quantum interference device (SQUID) loop, allowing frequency tuning using a flux-bias Z control line.[13,14] Excitation pulses are through a separate XY control line and readout uses a quarter-wave coplanar resonator dispersively coupled to the qubit, probed by a readout transmission line.[15] Control and readout lines for the qubit on the smaller die are located on the larger control die. All the galvanic control and readout connections are made using Al wire bonds to bond pads on the periphery of the control die. Signals are coupled to the flipped die using vacuum-gapped fixed inductive and capacitive couplers, shown in the equivalent circuit in panel (e). Using this assembly, we demonstrate quantum control and single-shot readout of each qubit, high-fidelity two-qubit entanglement, as well as a controlled-Z gate between the two qubits, which we characterize using quantum process tomography and randomized benchmarking.

The qubits on the two dies are coupled to one another through direct vacuum–gapped inductive coupling, achieved by aligning sections of coplanar transmission line with a 10 μm wide center trace and a 50 μm gap on each die (see Fig. 1). Each transmission line is shorted to ground on one end and connected to the SQUID loop of its respective qubit at the other end. The coupling inductors overlap when the flip-chip is assembled, a method that gives large and reliable mutual coupling between the elements on each die.[16,17]

Unique to the device here is the control line geometry for *Q*2, with no galvanic ground to the flipped die. This qubit, which also includes a two-junction SQUID loop, is tuned using a Z-control transmission line shorted to ground, located on the control die directly beneath *Q*2's SQUID loop, inductively coupled with a design inductance of $\approx$3 pH. The qubit is excited using on-resonant pulses coupled via a second XY-control transmission line terminated in an open circuit, located on the larger die beneath the capacitive cross of *Q*2, capacitively coupled with a design capacitance of $\approx$13 aF. The shape and location of these control lines, which sets their coupling strength, are determined using finite element simulations (Sonnet Software, Syracuse, NY). We use unique inductive qubit–qubit coupling and inductive coupling between the bottom die readout line and the flipped die *Q*2 readout resonator; see Table I. Simulations suggest that small flip-chip alignment errors do not contribute significantly.[11] For the qubit–qubit coupling of interest here, simulations indicate that a misalignment by 2 μm in the lateral directions alters the coupling by at most 2%, while a height offset of 0.5 μm alters the coupling by at most 3%.

The device was operated on the mixing plate of a dilution refrigerator with a base temperature of 7 mK. Control and readout uses custom electronics coupled through heavily filtered and attenuated (for control signals) coaxial cables. Readout signals are amplified by a traveling wave parametric amplifier[18] (TWPA) followed by a 4 K cryogenic amplifier; see Ref. 15 for more details. In Fig. 2(a), we show the microwave transmission through the readout line, with the two readout resonators visible as dips in transmission at 5.5 and 5.6 GHz. The dip at 6.4 GHz is due to the TWPA. Inflections at 3.5 and 7.5 GHz are due to filters and amplifier bandwidths. We do not observe any extra box- or slot-mode resonances due to the flip-chip geometry. Modeling the geometry as a rectangular microstrip antenna, we calculate the lowest frequency resonant mode for the $2 \times 4\,\text{mm}^2$ flipped die to be at $\approx$37 GHz, well above the frequencies used here. Larger flipped dies reduce the resonant frequency, for example, for a $20 \times 20\,\text{mm}^2$ die; the lowest resonance would be at $\approx$7.5 GHz.[19]

We can excite the qubits using a resonant microwave pulse applied to their XY control lines on the control die. Readout of the qubit state is performed by probing the dispersively coupled readout resonator.[20–22] This coupled resonator shows a shift in its resonance frequency when the qubit is excited, shown for *Q*2 in Fig. 2(b). After exciting the qubits, we can monitor their decay to the ground state, yielding the qubit energy lifetime T_1, shown in Fig. 2(c), where fits yield $T_1 = 8$ and 16 μs for *Q*1 and *Q*2, respectively. We observe a residual thermal population in *Q*2 of about 10%, possibly due to poor thermalization, as this chip is thermally connected only by photoresist adhesive.

TABLE I. Qubit parameters and fidelities for single-qubit gates as well as the two-qubit controlled-Z gate. All gates are measured with randomized benchmarking.

Parameter	Qubit 1	Qubit 2
Designed qubit capacitance (fF)	88	88
SQUID inductance (nH)	12.1	13.5
Qubit maximum frequency (GHz)	4.65	4.39
Qubit anharmonicity, α (MHz)	−179	−190
Qubit lifetime, T_1, at maximum frequency point (μs)	7.7 ± 0.1	17.3 ± 0.1
Qubit lifetime, T_1, at operating point (μs)		16.4 ± 0.1
Qubit Ramsey dephasing time, T_2, at max frequency (μs)	10.1 ± 0.2	7.5 ± 0.1
Qubit Ramsey dephasing time, T_2, at operating point (μs)		1.6 ± 0.1
Readout resonator frequency (GHz)	5.46	5.63
Designed qubit–readout resonator coupling (MHz)	35	35
Designed readout dispersive shift (MHz)	0.14	0.12
Measured readout dispersive shift (MHz)	0.2	0.1
Designed qubit–qubit coupling (MHz)		13
Measured qubit–qubit coupling (MHz)		12

Single qubit gate	Duration	Qubit 1 fidelity	Qubit 2 fidelity
I	50 ns	0.998 0 ± 0.000 3	0.997 1 ± 0.000 4
X/2	25 ns	0.997 7 ± 0.000 1	0.997 9 ± 0.000 3
−X/2	25 ns	0.997 4 ± 0.000 1	0.998 3 ± 0.000 5
Y/2	25 ns	0.998 3 ± 0.000 1	0.997 7 ± 0.000 4
−Y/2	25 ns	0.998 1 ± 0.000 1	0.997 1 ± 0.000 5
Z/2	25 ns	0.998 3 ± 0.000 1	0.999 5 ± 0.000 3
X	50 ns	0.996 7 ± 0.000 1	0.993 2 ± 0.000 5
−X	50 ns	0.996 5 ± 0.000 2	0.996 4 ± 0.000 3
Y	50 ns	0.996 6 ± 0.000 1	0.994 8 ± 0.000 5
−Y	50 ns	0.997 6 ± 0.000 2	0.997 1 ± 0.000 4
Z	25 ns	0.998 4 ± 0.000 1	0.999 3 ± 0.000 4
H	50 ns	0.996 3 ± 0.000 2	0.996 7 ± 0.000 5

Two qubit gate	Duration	Fidelity
Controlled Z	40 ns	0.940 ± 0.007

We perform a Ramsey experiment with a small detuning, shown in the lower panel of Fig. 2(c), to measure the qubit's energy coherence time T_2. Fitting yields $T_2 = 10$ and 2 μs for $Q1$ and $Q2$, respectively, measured at the operating point for the CZ gate, with $Q1$ at its maximum frequency point and $Q2$ flux-biased away from its maximum frequency. An independent measurement of $Q2$ performed at its maximum frequency point yields $T_2 = 7$ μs. These times are in line with our standard (non-floating) qubits, where we find T_1 times of order $5 - 20$ μs and operating point T_2 times of order $0.5 - 2$ μs.

We also tune up single qubit rotations for both qubits and benchmark the standard single qubit gates using randomized benchmarking,[23] as shown in Table I. We find the fidelity of all single qubit rotations to be well above 0.99.

We next investigate controlled interactions between the two qubits. By first exciting one qubit and then bringing the qubits into frequency resonance, we can swap states between them. By varying the amount of time that the two qubits are tuned into resonance, we can observe Rabi swaps, shown in Fig. 3(a). We perform two-qubit state tomography[24] to extract density matrices for our system and can calculate fidelities from the trace distance to the ideal state density matrices. The density matrices of the two-qubit state before and after a full swap are shown in Figs. 3(b) and 3(c); we find a state fidelity of 0.96 ± 0.02 for the two-qubit state before the swap and 0.94 ± 0.01 after the swap. By tuning the qubits into resonance for one-half of a full swap, we can generate a Bell state $(|ge\rangle - |eg\rangle)/\sqrt{2}$ between them. The Bell state density matrix measured using state tomography is shown in Fig. 3(d), with a state fidelity of 0.946 ± 0.005 after correcting for readout errors.[25] These results show that the flip-chip construct preserves good qubit performance and that we can separately control each qubit on the two dies as well as generate high-fidelity entanglement between the qubits.

A key gate for quantum computing is the controlled-Z (CZ) gate, in which a relative phase shift of π is acquired by the two-qubit $|ee\rangle$ state compared to the other states in the computational manifold. We implement this gate via an interaction of the $|ee\rangle$ state with the non-computational $|fg\rangle$ state, which can be brought into resonance with

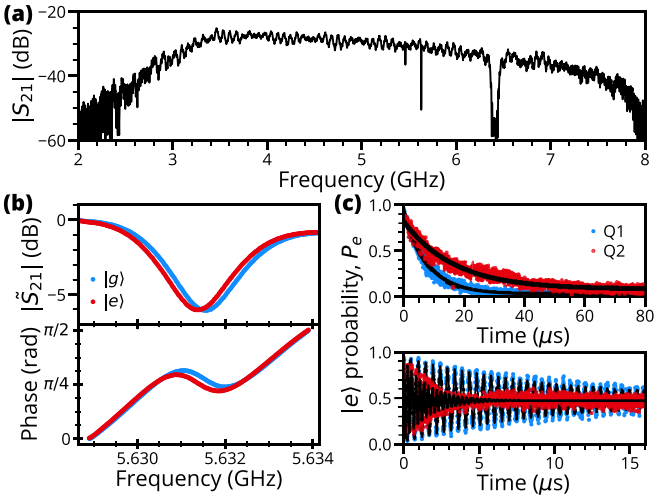

FIG. 2. Readout line transmission and qubit characterization. (a) Microwave transmission measurement of the readout line, showing the readout resonators at 5.5 and 5.6 GHz. Dip at 6.4 GHz is due to a traveling wave parametric amplifier; absolute scale is arbitrary. (b) Normalized transmission and phase of the dispersively coupled readout resonator with Q2 in its ground (blue) and excited (red) states. The dispersive shift of Q2 is about 0.1 MHz at its operating point. (c) T_1 lifetime (upper) and T_2 decoherence (lower) of Q1 (blue) and Q2 (red) measured at their operating points. To measure the qubits' energy lifetime T_1, we prepare the qubit in its first excited state $|e\rangle$ and measure the excited state probability P_e after a variable delay time. We find a fit exponential (black line) relaxation T_1 time of 8 and 16 μs for Q1 and Q2, respectively. We also observe a residual thermal population of 10% in Q2. A Ramsey fringe experiment yields Ramsey phase coherence T_2 times of 10 and 2 μs for Q1 and Q2, respectively (black lines). The lower T_2 time for Q2 is due to operation away from its maximum frequency point.

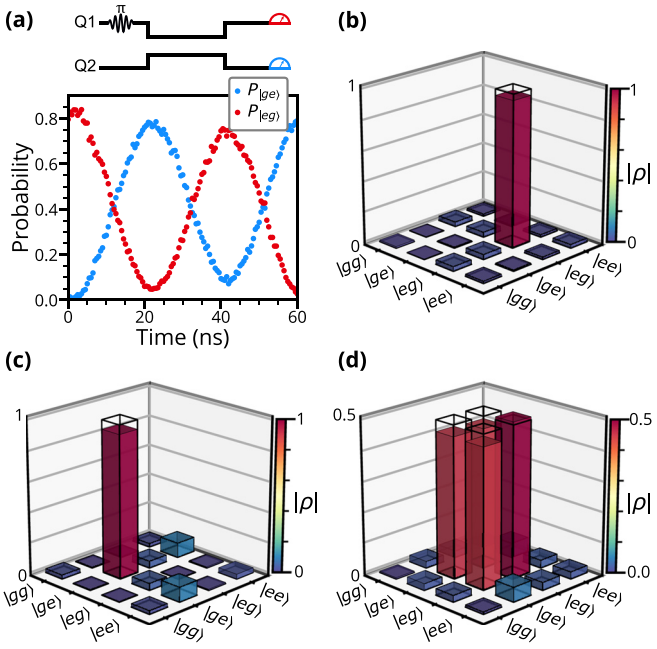

FIG. 3. Excitation swaps and Bell state preparation. (a) Excitation swaps between the qubits as a function of interaction time; control pulse diagram for the two qubits is shown above. (b) We excite qubit Q1 and perform state tomography of the resulting $|eg\rangle$ state. Density matrix element amplitudes are plotted. Colored bars show the experimental results and black outlines show the ideal state. The fidelity for this state, calculated as the trace distance to the ideal $|eg\rangle$ state, is 0.96 ± 0.02. (c) State tomography of the $|ge\rangle$ state, generated by exciting Q1 and performing a full swap between Q1 and Q2. The fidelity for this state is 0.94 ± 0.01. (d) State tomography of the Bell state $(|ge\rangle - |eg\rangle)/\sqrt{2}$, created by exciting Q1 and then performing a half-swap between the two qubits. The fidelity compared to the ideal Bell state is 0.946 ± 0.005. Qubit tomography includes corrections for measurement errors.[25]

the $|ee\rangle$ state using single-qubit Z-tuning pulses. To determine the parameters for this gate, we first perform qubit spectroscopy on Q1 at strong drive powers, revealing the energy eigenstates shown in Fig. 4(a). In this experiment, while applying a strong microwave tone to Q1 at a frequency shown on the vertical axis, we tune its frequency, shown on the horizontal axis, while leaving Q2's frequency fixed. We then measure the transmission of the readout line at a frequency close to Q1's readout resonator frequency, where the transmission increases when Q1 is excited to higher states. We calculate the eigenmode frequencies for the system, overlaid as black dashed lines in the figure, and find good agreement with the experimental data.

The critical avoided-level crossing for the CZ gate is between the $|ee\rangle$ and $|fg\rangle$ states, circled in Fig. 4(a). The CZ gate is implemented by applying a 30 ns-duration Z tuning pulse to Q1 and Q2, moving the $|ee\rangle$ state of the two-qubit system into an avoided-level crossing with $|fg\rangle$, thus enabling a full swap from $|ee\rangle$ to $|fg\rangle$ and back. This induces a phase change $|ee\rangle \rightarrow e^{i\pi}|ee\rangle$, leaving the other two-qubit states $|gg\rangle$, $|eg\rangle$ and $|ge\rangle$ unchanged.

The relative phase of the target $|ee\rangle$ state can be measured by performing Ramsey experiments on Q2 dependent on the state of Q1, as shown in Figs. 4(b)–4(d). In Fig. 4(b), no CZ tuning pulse are applied, and the Ramsey measurement of Q2 shows the expected non-interacting result. In (c), where CZ pulses are applied, we see that Q2's $|e\rangle$ state acquires a π phase shift if Q1 is in its $|e\rangle$ state; in Fig. 4(d), a set of additional pulses are added to compensate for phase accumulation during the gate.

We can calculate the CZ gate χ matrix, using $\varepsilon(\rho) = \sum_{mn} \tilde{E}_m \rho \tilde{E}_n^\dagger \chi_{mn}$, where ρ is the input density matrix and $\varepsilon(\rho)$ is the output density matrix.[26] Here $\tilde{E}$ is drawn from the basis of Pauli operators. We perform two-qubit process tomography[27] on the CZ gate; from the experimentally measured χ matrix, we calculate a final state fidelity of 0.947 ± 0.003 to the ideal χ matrix. We also use two-qubit randomized benchmarking to further characterize the CZ gate, by expanding our single-qubit benchmarking procedure to the two-qubit Clifford group.[28] By compared to a reference measurement taken without interleaved CZ gates, we calculate a benchmarking fidelity of 0.940 ± 0.007.

We have demonstrated the use of a non-galvanically connected flip-chip architecture with qubits on both a galvanically grounded control die and an electrically floating flipped die, showing full high-fidelity control of both qubits and coupling between qubits located on separate dies. We also show excitation swaps and high-fidelity two-qubit entanglement between the qubits, demonstrate a controlled-Z gate, and perform randomized benchmarking of single qubit gates as well as process tomography and two-qubit randomized benchmarking of the controlled-Z gate. We did not observe significant crosstalk

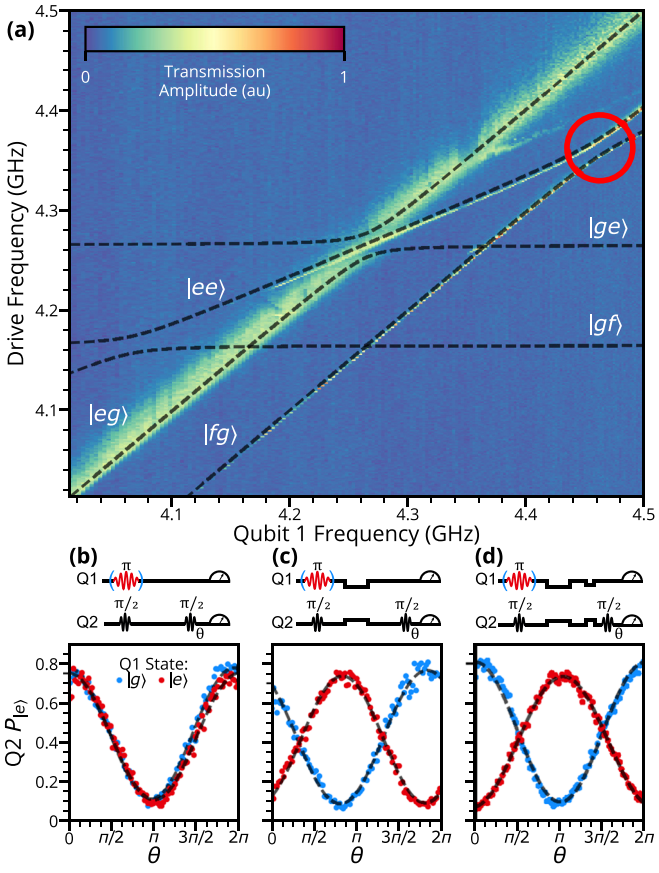

FIG. 4. Qubit spectroscopy and controlled-Z entangling gate. (a) Qubit spectroscopy. Qubit 2's frequency is held constant while Q1's frequency is tuned along the horizontal axis using its Z control line, and the drive frequency of an XY excitation tone applied to Q1 is varied along the vertical axis, while monitoring the readout transmission close to the frequency of Q1's readout resonator. When the drive tone excites the qubit, there is an increase in the transmission amplitude, due to a shift of the readout resonator's loaded frequency. With sufficient drive amplitude, both one- and two-photon processes are visible. Red circle indicates the CZ avoided-level crossing; overlaid dashed black lines are the calculated eigenmode frequencies for the different two-qubit states. (b) Ramsey experiment on Q2, with Q1 prepared in either the ground $|g\rangle$ or excited $|e\rangle$ state. Pulse sequence shown above; the qubits here do not interact. (c) Ramsey experiment as in (b) but with a 30 ns CZ gate pulse on the two qubits, enabling an interaction between the $|ee\rangle$ and $|fg\rangle$ states that generates a π phase shift on the $|ee\rangle$ state. (d) Ramsey experiment as in (c) but with additional small single-qubit tuning pulses following the CZ gate pulse, correcting the final qubit phase.

effects, but, of course, these may occur in more complex circuits. The architecture described here could prove useful for designing and implementing more complex superconducting qubit experiments, enabling a simplification of complicated wiring than could not easily be achieved using a single-die architecture.

The authors thank P. J. Duda for fabrication assistance. The authors thank MIT Lincoln Lab for providing a travelling-wave parametric amplifier (TWPA). Devices and experiments were supported by the Air Force Office of Scientific Research and the Army Research Laboratory. É.D. was supported by LDRD funds from Argonne National Laboratory; A.N.C. was supported in part by the DOE, Office of Basic Energy Sciences. This work was partially supported by the University of Chicago's MRSEC (NSF Award No. DMR-2011854) and made use of the Pritzker Nanofabrication Facility, which receives support from SHyNE, a node of the National Science Foundation's National Nanotechnology Coordinated Infrastructure (NSF Grant No. NNCI1542205), with additional support from NSF QLCI for HQAN (NSF Award No. 2016136).

DATA AVAILABILITY

The data that support the findings of this study are available from the corresponding author upon reasonable request.

REFERENCES

[1]M. H. Devoret and R. J. Schoelkopf, "Superconducting circuits for quantum information: An outlook," Science **339**, 1169–1174 (2013).
[2]G. Wendin, "Quantum information processing with superconducting circuits: A review," Rep. Progess Phys. **80**, 106001 (2017).
[3]F. Arute, K. Arya, R. Babbush, D. Bacon, J. C. Bardin, R. Barends, R. Biswas, S. Boixo, F. G. S. L. Brando, D. A. Buell *et al.*, "Quantum supremacy using a programmable superconducting processor," Nature **574**, 505–510 (2019).
[4]D. Rosenberg, S. Weber, D. Conway, D. Yost, J. Mallek, G. Calusine, R. Das, D. Kim, M. Schwartz, W. W *et al.*, "3D integration and packaging for solid-state qubits," arXiv:1906.11146 [quant-ph] (2019).
[5]A. Dunsworth, R. Barends, Y. Chen, Z. Chen, B. Chiaro, A. Fowler, B. Foxen, E. Jeffrey, J. Kelly, P. V. Klimov *et al.*, "A method for building low loss multi-layer wiring for superconducting microwave devices," Appl. Phys. Lett. **112**, 063502 (2018).
[6]J. Rahamim, T. Behrle, M. J. Peterer, A. Patterson, P. A. Spring, T. Tsunoda, R. Manenti, G. Tancredi, and P. J. Leek, "Double-sided coaxial circuit QED with out-of-plane wiring," Appl. Phys. Lett. **110**, 222602 (2017).
[7]J. H. Béjanin, T. G. McConkey, J. R. Rinehart, C. T. Earnest, C. R. H. McRae, D. Shiri, J. D. Bateman, Y. Rohanizadegan, B. Penava, P. Breul *et al.*, "Three-dimensional wiring for extensible quantum computing: The quantum socket," Phys. Rev. Appl. **6**, 044010 (2016).
[8]D. R. W. Yost, M. E. Schwartz, J. Mallek, D. Rosenberg, C. Stull, J. L. Yoder, G. Calusine, M. Cook, R. Das, A. L. Day *et al.*, "Solid-state qubits integrated with superconducting through-silicon vias," npj Quantum Inf. **6**, 59 (2020).
[9]M. Vahidpour, W. O'Brien, J. T. Whyland, J. Angeles, J. Marshall, D. Scarabelli, G. Crossman, K. Yadav, Y. Mohan, C. B *et al.*, "Superconducting through-silicon vias for quantum integrated circuits," arXiv:1708.02226 [physics.app-ph] (2017).
[10]B. Foxen, J. Y. Mutus, E. Lucero, R. Graff, A. Megrant, Y. Chen, C. Quintana, B. Burkett, J. Kelly, E. Jeffrey *et al.*, "Qubit compatible superconducting interconnects," Quantum Sci. Technol. **3**, 014005 (2018).
[11]K. J. Satzinger, C. R. Conner, A. Bienfait, H.-S. Chang, M.-H. Chou, A. Y. Cleland, E. Dumur, J. Grebel, G. A. Peairs, R. G. Povey *et al.*, "Simple non-galvanic flip-chip integration method for hybrid quantum systems," Appl. Phys. Lett. **114**, 173501 (2019).
[12]G. J. Dolan, "Offset masks for lift-off photoprocessing," Appl. Phys. Lett. **31**, 337 (1977).
[13]J. Koch, T. M. Yu, J. Gambetta, A. A. Houck, D. I. Schuster, J. Majer, A. Blais, M. H. Devoret, S. M. Girvin, and R. J. Schoelkopf, "Charge-insensitive qubit design derived from the Cooper pair box," Phys. Rev. A **76**, 042319 (2007).
[14]R. Barends, J. Kelly, A. Megrant, D. Sank, E. Jeffrey, Y. Chen, Y. Yin, B. Chiaro, J. Mutus, C. Neill *et al.*, "Coherent Josephson qubit suitable for scalable quantum integrated circuits," Phys. Rev. Lett. **111**, 080502 (2013).
[15]Y. P. Zhong, H.-S. Chang, K. J. Satzinger, M.-H. Chou, A. Bienfait, C. R. Conner, E. Dumur, J. Grebel, G. A. Peairs, and R. G. P. Povey, "Violating Bell's inequality with remotely connected superconducting qubits," Nat. Phys. **15**, 741–744 (2019).
[16]K. J. Satzinger, Y. P. Zhong, H. S. Chang, G. A. Peairs, A. Bienfait, M. H. Chou, A. Y. Cleland, C. R. Conner, E. Dumur, J. Grebel *et al.*, "Quantum control of surface acoustic-wave phonons," Nature **563**, 661–665 (2018).

[17]A. Bienfait, K. J. Satzinger, Y. P. Zhong, H.-S. Chang, M.-H. Chou, C. R. Conner, E. Dumur, J. Grebel, G. A. Peairs, R. G. Povey *et al.*, "Phonon-mediated quantum state transfer and remote qubit entanglement," Science **364**, 368–371 (2019).
[18]C. Macklin, K. O'Brien, D. Hover, M. E. Schwartz, V. Bolkhovsky, X. Zhang, W. D. Oliver, and I. Siddiqi, "A near–quantum-limited Josephson traveling-wave parametric amplifier," Science **350**, 307–310 (2015).
[19]G. Kumar and K. P. Ray, *Broadband Microstrip Antennas* (Artech House, Inc., 2003).
[20]D. I. Schuster, A. Wallraff, A. Blais, L. Frunzio, R.-S. Huang, J. Majer, S. M. Girvin, and R. J. Schoelkopf, "ac stark shift and dephasing of a superconducting qubit strongly coupled to a cavity field," Phys. Rev. Lett. **94**, 123602 (2005).
[21]A. Wallraff, D. I. Schuster, A. Blais, L. Frunzio, J. Majer, M. H. Devoret, S. M. Girvin, and R. J. Schoelkopf, "Approaching unit visibility for control of a superconducting qubit with dispersive readout," Phys. Rev. Lett. **95**, 060501 (2005).
[22]A. Blais, R.-S. Huang, A. Wallraff, S. M. Girvin, and R. J. Schoelkopf, "Cavity quantum electrodynamics for superconducting electrical circuits: An architecture for quantum computation," Phys. Rev. A **69**, 062320 (2004).
[23]E. Knill, D. Leibfried, R. Reichle, J. Britton, R. B. Blakestad, J. D. Jost, C. Langer, R. Ozeri, S. Seidelin, and D. J. Wineland, "Randomized benchmarking of quantum gates," Phys. Rev. A **77**, 012307 (2008).
[24]M. Steffen, M. Ansmann, R. McDermott, N. Katz, R. C. Bialczak, E. Lucero, M. Neeley, E. M. Weig, A. N. Cleland, and J. M. Martinis, "State tomography of capacitively shunted phase qubits with high fidelity," Phys. Rev. Lett. **97**, 050502 (2006).
[25]M. Ansmann, H. Wang, R. C. Bialczak, M. Hofheinz, E. Lucero, M. Neeley, A. D. O'Connell, D. Sank, M. Weides, J. Wenner *et al.*, "Violation of Bell's inequality in Josephson phase qubits," Nature **461**, 504–506 (2009).
[26]M. A. Nielsen and I. L. Chuang, *Quantum Computation and Quantum Information* (Cambridge University Press, 2000).
[27]M. Ansmann, M. Hofheinz, E. Lucero, M. Neeley, A. D. O'Connell, D. Sank, H. Wang, J. Wenner, M. Steffen, A. N. Cleland *et al.*, "Quantum process tomography of a universal entangling gate implemented with Josephson phase qubits," Nat. Phys. **6**, 409–413 (2010).
[28]R. Barends, J. Kelly, A. Megrant, A. Veitia, D. Sank, E. Jeffrey, T. C. White, J. Mutus, A. G. Fowler, B. Campbell *et al.*, "Superconducting quantum circuits at the surface code threshold for fault tolerance," Nature **508**, 500–503 (2014).